Mean pressure gradient effects on the performance of ramjet cavity stabilized flames

Anthony J. Morales [a], David M. Smerina [a], Mason.R. Thornton [a], Cal J. Rising [b], Jonathan Sosa [b], Ryan F. Johnson [c], David A. Kessler [c], Gabriel Goodwin [b], Kareem A. Ahmed [a],*

[a] Center for Advanced Turbomachinery and Energy Research, Department of Mechanical and Aerospace Engineering, University of Central Florida, Orlando, FL, 32816, United States
[b] Naval Center for Space Technology, U.S. Naval Research Laboratory, Washington DC, 20375, United States
[c] The Laboratories for Computational Physics & Fluid Dynamics, U.S. Naval Research Laboratory, Washington DC, 20375, United States

A R T I C L E   I N F O

A B S T R A C T

Premixed cavity stabilized flames are experimentally investigated in a high-speed ramjet engine under the influence of varying mean pressure gradients. The ramjet cavity incorporates a backward facing step with an aft ramp for flame stabilization in high Reynolds number. The ramjet engine is subject to varying wall geometry to form converging, diverging, and nominal configurations in order to investigate the effects of mean pressure gradients on engine performance. High-speed particle image velocimetry (PIV) and chemiluminescence imaging diagnostics are simultaneously employed to capture the reacting flow fields and flame dynamics. Imposing a larger favorable pressure gradient is shown to shrink the recirculation zone and alter shear layer dynamics, which leads to increased drag on the cavity. Additionally, inducing a stronger favorable pressure gradient is shown to excite a shear layer instability mode, characterized by a Strouhal number of $St = 0.1$. Proper orthogonal decomposition (POD) results reveal that the instability mode is comprised of large-scale oscillations that occupy the entire cavity flow region, indicating that the excited oscillations are the manifestation of a global vortex shedding instability that occurs under non-reacting conditions. The results demonstrate that the performance and stability of the ramjet cavity flame can be influenced by the mean pressure gradient, which is vital for the design of high-speed air-breathing propulsion systems such as dual-mode scramjets.

1. Introduction

There remain considerable efforts to develop advanced and robust propulsion systems for supersonic and hypersonic flight applications. Development efforts are geared toward high-speed aircraft which can operate safely and efficiently over a wide range of flight conditions [1,2]. An example of a promising technology is a dual-mode scramjet (DMSR), which is designed to fly from supersonic (Mach ≈ 2–3) to hypersonic speeds (Mach > 5) [3,4]. In addition to the versatile operating range, DMSR systems offer a lightweight design, reduced heat load, and higher specific thrust. However, one of the primary challenges of DMSR engines is combustion stability. In particular, the combustion process must be sustained in both subsonic (ramjet-mode) and supersonic (scramjet-mode) flows. De-

veloping combustors to effectively handle the wide range of flow conditions is challenging due to turbulence and compressibility effects, which will influence flame stability, chemical reactivity, and propulsive performance [5]. For these reasons, additional studies of flame stabilization in high-speed flows are needed to aid the development of next-generation propulsion systems.

One of the primary challenges of dual-mode combustors is flame stabilization [6]. In particular, high flow velocities coupled with small flow timescales, short mixing length, and intense turbulence make continuous ignition and flame stabilization challenging. High flow velocities will induce mean shear along the flame due to intense turbulence and mixing effects [7,8]. This has the potential to cause reaction instabilities and make the flame more prone to destabilization or blowout [5,9,10], which is detrimental for air-breathing propulsion systems. Additional variables, such as pressure, temperature, and fuel injection scheme will also alter ignition [11–14], flame stability [15–18], and blowout limits [5,9,10,19,20]. Therefore, optimizing the design of the flame stabilization mecha-

* Corresponding author.
    E-mail addresses: anthony.morales@ucf.edu (A.J. Morales),
kareem.ahmed@ucf.edu (K.A. Ahmed).

nism is critical to ensure reactions can be sustained across a wide range of high-speed flow conditions [21,22]. Many flame stabilization mechanisms have been investigated in the literature, including backward facing steps [23,24], bluff bodies [25–27], gutters [28], ramp/struts [29–33], and cavities [34]. Amongst the stabilization mechanisms, cavity configurations are the most promising candidate for stabilizing flames in both supersonic and subsonic streams [5,35]. A cavity configuration provides a recirculation zone to trap hot combustion products, which allows for flames to be stabilized through the continuous preheating and ignition of inflowing reactants [29,36]. Additionally, the geometry of the cavity provides lower drag penalties relative to other common stabilization mechanisms [37].

One of the main design considerations for cavities is the length/step height ratio (L/H), which influences flame stability limits, self-sustained oscillations, and pressure losses [5,21,29]. For all cavities, a shear layer will develop and separate from the upstream lip and reattach itself downstream. Long and shallow cavities with $L/H > 10$–13 are categorized as closed cavities, and the shear layer will reattach to the lower wall of the cavity [30,38]. Shear layer reattachment on the lower wall imposes high pressure forces on the downstream wall regions, and results in large drag losses. Drag losses can be reduced for open cavities, defined as $L/H < 7$–10, which decreases the axial length of shear layer reattachment. However, open cavities are prone to self-sustained oscillations, which causes fluctuations in the pressure, density, and velocity, which can result in high drag penalties. Furthermore, cavity oscillations (either longitudinal or transverse) will dictate aerodynamic and thermoacoustic instabilities, and thus are relevant to ensure flames can be stabilized over a wide operability range. For this reason, various strategies have been proposed to control cavity oscillations, including an angled back wall (or ramp) [5,30], which mitigates shear layer oscillations relative to a 90° step. Finally, it is important to note that cavity oscillations are most sensitive in subsonic flow regimes, where fluctuations in mean velocity, turbulence, or mixture fraction can heavily influence the oscillation frequency and resonant instability modes [39,40]. This becomes relevant during the first stage of dual mode engine operation (i.e. ramjet-mode), in which the inlet flow to the cavity will be subsonic. Thus, further investigations of open cavity oscillations, particularly in subsonic flow regimes, can guide optimized design strategies to enhance cavity combustion for dual mode scramjets.

Previous studies have provided many insights regarding the dynamics of cavity stabilized flames for propulsion applications. The current research builds upon the literature and experimentally investigates the influence of mean pressure gradients on the combustion performance, drag, and self-sustained oscillations of a cavity stabilized dual-mode scramjet combustor. The mean pressure gradient is altered by adjusting the angle of the channel wall opposite the cavity. The flame position and flow field are quantified with simultaneous high-speed PIV and chemiluminescence diagnostics. The results demonstrate that the cavity dynamics can be tailored via the mean pressure gradient, which ultimately provides an avenue to optimize the performance of high-speed air-breathing propulsion systems.

2. Materials and methods

2.1. Experimental facility

Experiments were performed at the Propulsion and Energy Research Laboratory (PERL), at the University of Central Florida (UCF). A cavity is integrated into a high-speed dual-mode scramjet combustor, shown in Fig. 1. A premixed reacting flow composed of a mixture of ethylene (C_2H_4) and air is explored in an optically
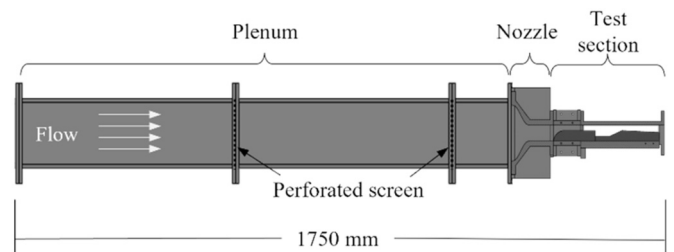

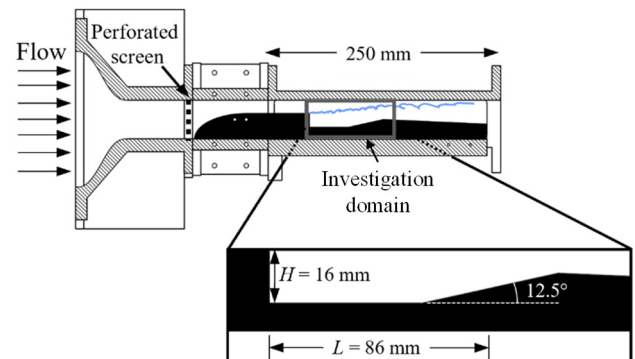Fig. 1. Schematic of premixed cavity ramjet facility.

Fig. 2. Optically accessible test section and ramjet cavity flameholder.

accessible test section exhausting to atmospheric conditions. The mixture enters a 0.5 m long, 3-in diameter pipe, which expands into a 1.5 m long, 130 mm × 155 mm rectangular plenum. Flow conditioning is performed at separate locations in the rectangular plenum using screens with a 4 mm square mesh, ensuring a uniform flow-field at the plenum exit. A transitional nozzle connects the plenum and the main optically accessible-test section, accelerating the flow to the desired conditions.

A schematic of the nozzle and the cavity flameholder is provided in Fig. 2. The neck of the nozzle has a cross section of 127×45 mm, and a third 4 mm square mesh perforated screen is placed at the outlet of the nozzle, prior to the combustor inlet channel. Before the cavity, a rounded body is used to create a 15 mm height channel that extends 73 mm upstream of the cavity. The channel leads into the cavity section, which consist of a backward facing step with an aft ramp. The step has a height of $H = 16$ mm, which corresponds to an expansion ratio of ~2:1 based on the inlet channel height. Following the step is an aft ramp, which has an inclined angle of 12.5° relative to the cavity floor. The cavity length, defined as the axial distance from the rearward facing step to the center of the aft ramp [30,38], is $L = 86$ mm, which corresponds to an $L/H = 5.4$. The tallest point of the aft ramp is 7 mm below the height of the step, which provides a relief angle of 2.5 degrees from the corner of the step. The relief angle of 2.5° continues past the ramp inflection point to the end of the test section. The cavity and downstream section span the width of the test section. A spark plug positioned on the lower wall of the cavity interior is used to ignite the fuel-air mixture.

The opposing wall of the cavity and side walls are recessed and fitted with fused silica quartz glass for optical access. The glass provides 95% transmissibility across the 250–700 nm range. Additionally, to reduce near-wall laser-light scattering, the cavity is painted with non-reflective black paint. The top wall can be modified using a $+/-$ 3-degree wedge to induce varying pressure gradients within the test section: a nozzle, nominal, and diffuser configuration as shown in Fig. 3. The mean pressure gradients are calculated through flow field measurements, and are presented in the later sections.
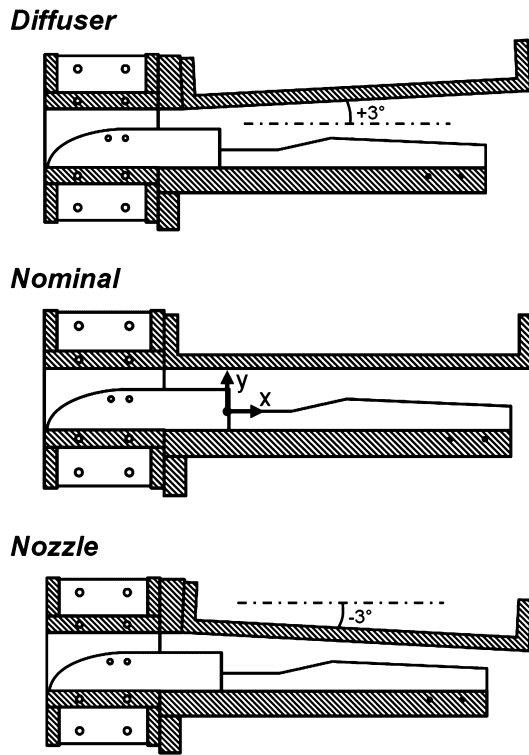
Diffuser

Nominal

Nozzle

Fig. 3. Cavity configurations used to tailor the mean pressure gradient. The coordinate axis used in this study is also included on the nominal configuration.

2.2. Flow metering and controls

A Fisher 546NS Electro-Pneumatic valve regulates a large high-pressure reservoir of 300 K air to approximately 90 psi and controls mass flow rate into the facility via a sonic orifice with a diameter of 12.7 mm, located upstream of the plenum. A Dwyer 626 (0–300 psi) pressure transducer with an accuracy of 0.25% of the full-scale range is located before the orifice and is used to meter the air flow rate. Pressure measurements are acquired in LabVIEW software, which incorporates a feedback loop with a PID controller to regulate the Fisher valve to the desired upstream pressure. The pressure measurements and feedback systems ensure that all experiments are conducted with the desired inlet channel velocity of $u_\infty = 85$ m/s, corresponding to a Mach number of $Ma \approx 0.25$.

Ethylene gas and air are introduced into a 3-way steel pipe fitting well before the conditioning plenum to allow thorough premixing. The upstream fuel pressure is regulated in-line and is metered by an O'Keefe precision orifice with a diameter of 3.175 mm. The upstream fuel pressure is measured by a Dwyer 628 (0–1500 psi) pressure transducer, with an associated accuracy of 1% of the full-scale range. Similarly, a swirl seeder injects 3 μm alumina powder (Al_2O_3) seed particles shortly downstream of the fuel and air. The seed is driven by a separate air supply at a constant 115 psi and modulated through an in-line regulator. The seed air is metered through a 3.048 mm O'Keefe precision orifice and measured using an identical Dwyer 628 (0–1500 psi) pressure transducer. Fuel and seed issued into the airflow is controlled via Burkert and U.S. Solid electric solenoid valves using NI LabVIEW.

2.3. High-speed optical diagnostics

The flame and flow field is characterized using simultaneous high-speed broadband chemiluminescence and two-dimensional particle image velocimetry (PIV). PIV measurements were performed by illuminating the 3 μm alumina particles using a 532 nm,

dual-head, ND:YAG laser (LDP-200MQG Dual). 20 kHz PIV images are collected in a frame straddled mode, where each laser head is independently pulsed at 20 kHz, and the time delay between the two laser pulses is $dt = 5$ μs. The laser beams are directed through sheet forming optics, which consist of a 1000 mm focusing lens and a -25.4 mm cylindrical lens to create a thin sheet. The laser sheet is then projected through the bottom glass by a mirror and centered in the spanwise (z) dimension of the test section. Seed particle movement is captured using a high-speed CMOS camera (Photron Fastcam SA-Z 2100 K) with a 50–300 mm adjustable focal length lens. A BNC model 575 pulse/delay generator was used to synchronize and trigger the lasers and camera diagnostic systems.

The investigation domain used for this study is highlighted in Fig. 2. The domain is selected to optimize the spatial resolution of the images at the high acquisition rate while still viewing the entire cavity region. The cavity domain has a 100×50 mm field of view with a 1024×512 pixel resolution for an imaging resolution of 98 μm/pix. All PIV images are processed in LaVision DaVis 8 software. The initial interrogation window is set to 64×64 pixels with 3 passes and a 50% overlap. The final window is reduced to 8×8 pixels, also with 3 passes and a 50% overlap. The final window size was selected to maximize the vector resolution according to best practices without jeopardizing correlation-based uncertainties in the processing algorithm [41]. The final window size corresponds to a measurement resolution of 781 μm, and the 50% overlap gives a vector spacing of $\lambda_m = 391$ μm.

The vector spacing is well resolved with respect to the flame thickness, $\lambda_m/l_f = 1.3$, and l_f is the laminar flame thickness of a premixed ethylene-air flame at an equivalence ratio of one ($\Phi = 1$) [42]. With respect to the turbulence length scales, the vector spacing is $\lambda_m/l_0 \approx 0.05$ and $\lambda_m/l_k \approx 2.4$, where l_0 and l_k are the integral and Kolmogorov length scales, respectively, and l_k is calculated from dimensional arguments as $l_k = l_0(u'_{rms}l_0/\nu)^{-1/2}$ [43,44]. Dimensional arguments are also used to calculate the Kolmogorov timescales, $\tau_k = \tau_0(u'_{rms}l_0/\nu)^{-1/2}$, where τ_0 is the integral timescale, $\tau_0 = l_0/u'_{rms}$. The Kolmogorov timescale is used to estimate the maximum characteristic angular frequency of turbulence, $\omega_c = 1/\tau_k$, which is subsequently used to quantify the Stokes number, $St = d_p(\omega_c/\nu)^{1/2} = 0.12$ [45]. The experimental conditions and processing method result in a maximum velocity uncertainty of 0.45 m/s based on correlation statistics [46].

Broadband chemiluminescence measurements are used to identify the heat release regions and outline the flame front. 20 kHz images are recorded using a high-speed CMOS camera (Photron Fastcam SA1.1 675 K), equipped with a Nikon 50 mm $f/1.2$ lens. The camera had a single field of view of 128×74 mm with a 640×368 pixel resolution, corresponding to an image resolution of 200 μm/pix.

2.4. Flame front extraction

The flame front contours can be identified from either the chemiluminescence images or the mie scatter images obtained from PIV. For this study, the chemiluminescence images are used to quantify the time-averaged location of the flame front since the images provide a line-of-sight view of the heat release regions. However, instantaneous flame structures were obtained from the mie scatter images from the PIV diagnostic. The mie extracted flame front contours are beneficial since they come from the same measurement plane as the velocity vectors, but also are useful for capturing small-scale turbulent flame structures [47–49]. The same methodology was used to extract flame coordinates from both image sets. Similar to previous work [50,51], the method relies on finding an appropriate intensity threshold to isolate the flame front coordinates. To do so, the images are first preprocessed with a $3 \times$

Table 1
Testing conditions.

Configuration	dp/dx (kPa/m)	u'_{rms} (m/s)	u'_{rms}/u_∞	l_0 (mm)	Da
Diffuser	3.9	4.9	0.058	7.9	3.57
Nominal	−0.8	4.4	0.052	7.5	3.77
Nozzle	−6.7	3.7	0.044	6.7	4.01

3 pixel median filter eliminate background noise. The threshold is then determined using Otsu's method [52], which calculates a statistical based threshold to isolate the flame region from the dark background. The image is then binarized about this threshold, and the mean flame coordinates are extracted from a boundary detection algorithm [53].

2.5. Testing conditions

The experimental conditions explored in this work are summarized in Table 1. All cases are subjected to the same inlet conditions, which consist of a premixed ethylene-air mixture at an equivalence ratio of one ($\Phi = 1$). The mean velocity in the inlet channel upstream of the step is held constant at $u_\infty = 85$ m/s, which corresponds to a Reynolds number $Re = u_\infty H/\nu = 91,000$. The influence of mean pressure gradients is explored by changing the upper wall geometry, as shown in Fig. 3. For each configuration, the mean axial pressure gradient (dp/dx) is quantified by inverting the streamwise fluid momentum equation, provided in index notation in Eq. (1). Here, p is pressure, V is the velocity vector, ρ is the density, and μ is the dynamic viscosity. All first and second order derivatives are calculated from the velocity vector fields, and the density and viscosity are that of air at 298 K. The mean pressure gradient is then calculated at all locations in the freestream reactant portions of the domain, and a spatial average is provided in Table 1.

$$\frac{\partial p}{\partial x_i} = -\rho \frac{\partial V_i}{\partial t} - \rho V_j \frac{\partial V_i}{\partial x_j} + \mu \frac{\partial^2 V_i}{\partial x_j^2} \qquad (1)$$

Based on the mean pressure gradients in Table 1, it is first noted that the diffuser case sustains an adverse pressure gradient in the freestream. This is due to flow expansion effects caused by the expansion ratio at the step along with the increasing cross-sectional area in the streamwise (x) direction. The expansion effects result in a slight decrease in the freestream flow velocity across the cavity, which will be highlighted in the results section. In contrast, both the nominal and nozzle configurations experience favorable pressure gradients, and the flow undergoes an axial acceleration in the freestream.

The corresponding freestream turbulence conditions for each test condition are also provided in Table 1. All turbulence properties were ensemble averaged in the reactant regions. The turbulent velocity fluctuations were calculated using Eq. (2), and the integral length scales were calculated using the two-point autocorrelation provided in Eq. (3). The turbulence quantities are then used to quantify the Damköhler number (Da), which captures the ratio of turbulence to flame timescales, presented in Eq. (4). Here, l_f is the laminar flame thickness, acquired from ref. [42], and s_l is the laminar flame speed, which is available from refs. [54–56].

$$u'_{rms} = \left[\frac{1}{N-1} \sum_{i=1}^{N} \left(u(t_N) - \bar{u} \right)^2 \right]^{1/2} \qquad (2)$$

$$l_0 = \int_{y_{min}}^{y_{max}} \frac{u'(x, y_0) u'(x, y)}{u'(x, y_0)^2} dy \qquad (3)$$

$$Da = \frac{\tau_{flow}}{\tau_{chem}} = \frac{(l_0/u'_{rms})}{(l_f/s_l)} \qquad (4)$$

3. Results

The following section presents the experimental results from the premixed cavity flames subjected to mean pressure gradients. The configurations explored are summarized in Table 1. The first section of the results analyzes means flame and flow properties to understand the effect of the pressure gradient on cavity performance. All results presented in this section are calculated from time-averaged data sets with over 5000 instantaneous samples. The subsequent section focuses on temporal dynamics including the self-sustained cavity oscillations and the implications on cavity drag for propulsion systems.

3.1. Performance characteristics

Time-averaged contours of streamwise velocity (u) and spanwise vorticity (ω_z) for each test configuration are provided in Fig. 4. The mean flame front, determined from the chemiluminescence images, is also overlaid onto the contours. For all cases explored here, the mean position of the flame front shows that all flames are shear stabilized [40,57], and inflowing reactants are continually ignited in the shear layers. The burned products are then advected into the recirculation zone, where they propagate back towards the upstream shear layers to reignite fresh inflowing reactants.

With regards to the flow field, changing the wall geometry alters the flow path as shown from the streamlines in the freestream portion of the domain. The streamlines for the diffuser tend to be deflected away from the cavity region, while the streamlines for the nozzle case impinge toward the aft ramp. The decrease in cross-sectional area for the nozzle results in the largest flow velocities compared to the other cases, which corresponds to the mean pressure gradients in Table 1. Progressing toward a stronger favorable pressure gradient leads to higher streamwise velocities; most notably, immediately downstream of the inflection point. For instance, the nozzle experiences strong flow acceleration immediately downstream of the inflection point, with streamwise velocities reaching values ~1.5 times larger than the inlet. Note that the largest streamwise velocities are also observed on the products side of the flame, which is expected due to the increase in temperature and decrease in fluid density in the products.
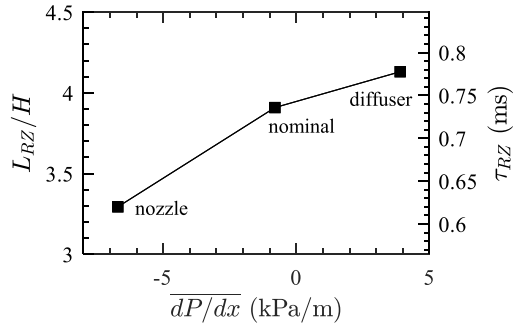
The mean pressure gradient and directionality of the streamlines also influence the size of the recirculation zone and the shear layer reattachment point. Here, the boundary of the recirculation zone is defined as the $u = 0$ contour, which is displayed for all cases in Fig. 4. This boundary is used to quantify the length of the recirculation zone (L_{RZ}), defined as the axial length from the step to the furthest x-position where the $u = 0$ contour intersects the aft ramp. The result is presented in Fig. 5, where the length of the recirculation zone decreases when progressing toward a larger favorable pressure gradient. The recirculation zone boundary in Fig. 4 also matches the trajectory of the shear layer, and thus the recirculation zone length is also a reliable marker to quantify the shear layer reattachment point on the aft ramp, which is an important characteristic for cavity performance and oscillations [29].

The corresponding recirculation zone residence time, $\tau_{RZ} = L_{RZ}/u_\infty$ [10], is also quantified and presented in Fig. 5. The recirculation zone residence time is significant in regard to flame stabilization. Based on perfectly stirred reactor models, flame blowout will occur when the reaction time exceeds the recirculation zone residence time [5]. In this case, the decrease in recirculation zone residence time with the transition toward a stronger favorable
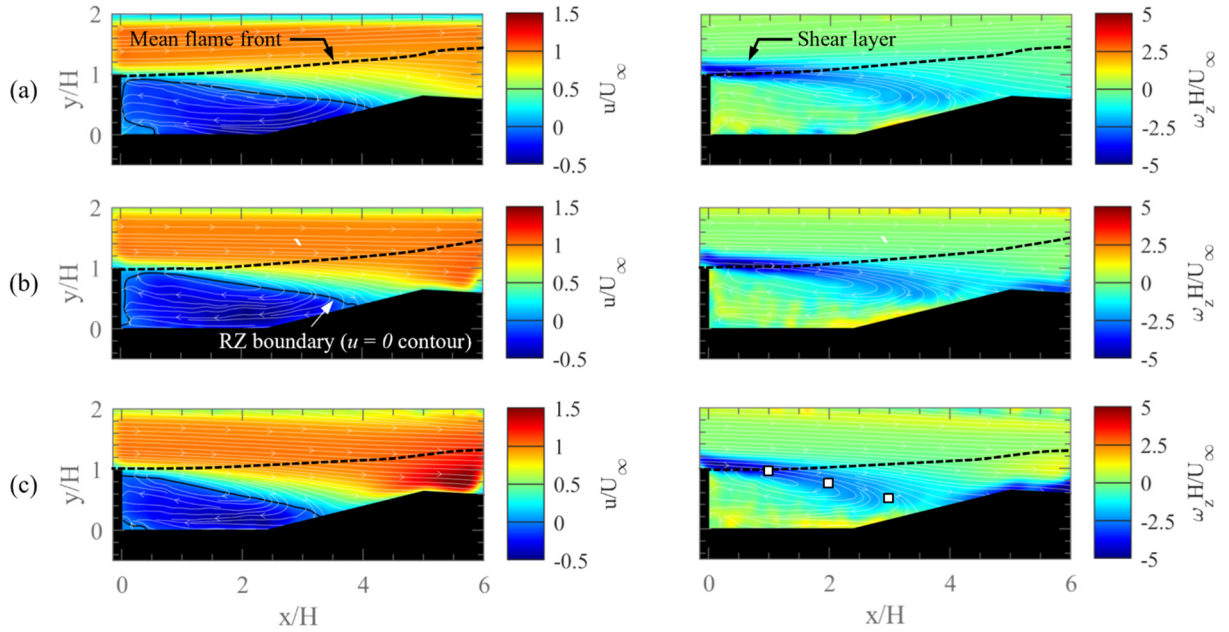
Fig. 4. Time-averaged streamwise velocity (u) and spanwise vorticity (ω_z) contours, including the mean flame front (dashed lines) and streamlines: (a) diffuser, (b) nominal, (c) nozzle. The white squares in the bottom right contour are the locations used for shear layer analysis discussed in later sections. (For interpretation of the colors in the figure(s), the reader is referred to the web version of this article.)

Fig. 5. Time-averaged recirculation zone length and residence time as a function of the mean pressure gradient.
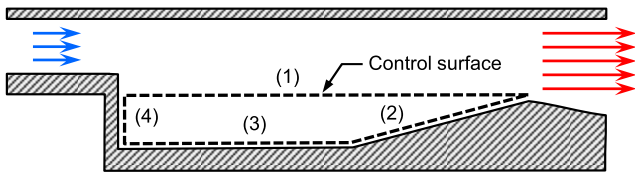
Fig. 6. Control volume used for momentum flux and drag analysis.

pressure gradient will minimize the amount of time the inflowing reactants interact with products in the recirculation zone [10]. This definition is analogous with a global Damköhler number, which theoretically predicts that flames cannot maintain stability if $Da = \tau_{flow}/\tau_{chem} < 1$.

The differences in recirculation zone and shear layer reattachment dynamics between the three test configurations are also expected to alter the drag on the cavity. To compare the cavity drag amongst trials, a control volume momentum flux analysis is conducted, similar to the approach from Gharib and Roshko [58]. A sketch of the control volume used for the analysis is provided in Fig. 6.

A momentum balance in the x-direction gives:

$$\sum F_x = \int_{cs} u\rho \left(\vec{V} \cdot d\vec{A} \right), \tag{5}$$

where the left-hand side of the equation accounts for all shear and pressure forces acting on the control volume (cv), and the right-hand side accounts for the streamwise momentum flux across all control surfaces (cs). Expanding the left-hand side of the equation gives:

$$-\int_{[1]} \tau dA + \int_{[2]} (pdA + \tau dA) + \int_{[3]} \tau dA - \int_{[4]} pdA = \int_{[1]} u\rho \left(\vec{V} \cdot d\vec{A} \right). \tag{6}$$

Here, the subscripted bracket numbers account for the specified control surface, and $\tau = \tau_{yx} = \mu(\partial v/\partial x + \partial u/\partial y)$ based on Newton's viscosity law [59]. Defining the cavity drag as the sum of all forces acting on the cavity walls [58] results in:

$$D = \int_{[2]} (pdA + \tau dA) + \int_{[3]} \tau dA - \int_{[4]} pdA$$

$$= \int_{[1]} u\rho \left(\vec{V} \cdot d\vec{A} \right) + \int_{[1]} \tau dA. \tag{7}$$

Therefore, the influence of the mean pressure gradient on the cavity drag can be evaluated by calculating the momentum flux and shear stress along control surface 1. In non-dimensional form, the drag coefficient is:

$$C_d = 2D/\rho u_\infty^2 A, \tag{8}$$

where A is the total surface area of the cavity walls, i.e., the combined length of control surface 2, 3, and 4 multiplied by the cavity depth in the z-direction.

The momentum flux terms across control surface 1 are calculated using the time-averaged velocity data, and the results are
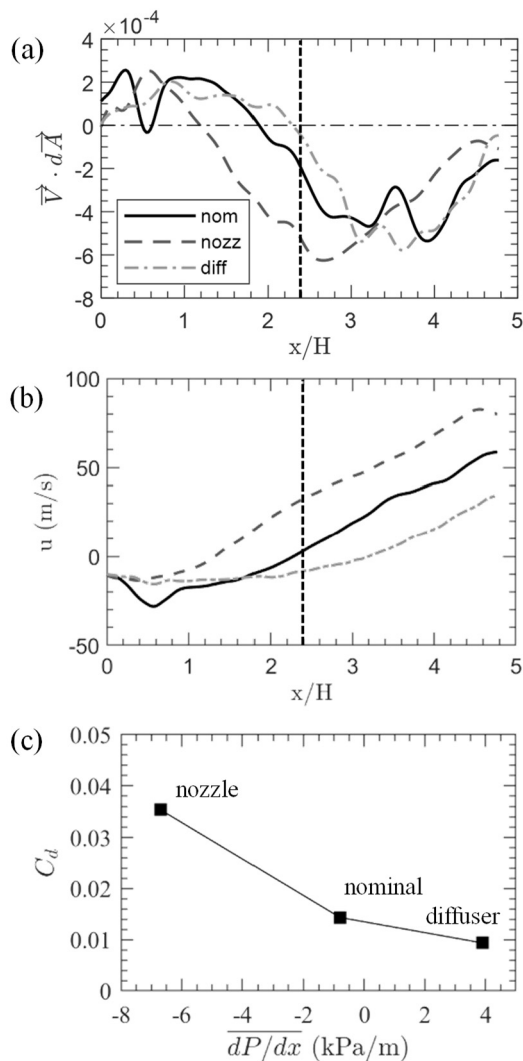
Fig. 7. (a) time-averaged velocity flux through control surface 1, (b) time-averaged velocity profiles along control surface 1, and (c) the drag coefficient for each test configuration. The vertical dashed line in (a) and (b) represent the location at the base of the aft ramp.

presented in Fig. 7 (a) and (b). The dot product in Fig. 7a represents flow entering (negative values) and leaving (positive values) the control volume. All curves depict the same trend where flow leaves the control volume near the cavity step, and the most significant flow entrainment occurs in the region between $x/H = 2.5$–4. Also, the transition from diffuser to nominal to nozzle shifts the curves upstream, which is representative of the shrinking recirculation zone and shear layer reattachment length as the conditions transition from an adverse to a favorable pressure gradient. Meanwhile, the profiles in Fig. 7b depict the time-averaged streamwise velocity taken along control surface 1. Since the flow is subsonic, increasing the mean pressure gradient leads to the nozzle sustaining the highest streamwise velocity along the control surface.

To quantify the total momentum flux across control surface 1, the product of the curves in (a) and (b) are combined with the mean fluid density [60], $\rho_{mean} = 0.5(\rho_u + \rho_b)$, where ρ_u and ρ_b are the unburnt and burnt gas densities, and the burnt gas density is calculated from NASAs chemical equilibrium calculator [61]. The momentum flux and shear stress profiles are then integrated along the control surface to calculate the drag coefficient, which is shown in Fig. 7c.

The transition to a strong favorable pressure gradient is accompanied with an increase in the drag on the cavity. This is due to: (1) the larger local velocities experienced in the nozzle, and (2) the orientation of the streamlines relative to the aft ramp. More specifically, the convergence of the streamlines toward the aft ramp for the nozzle will induce high pressure region along control surface 2 [29], and thus impart a greater drag penalty. The increase in local pressure along the aft ramp will decrease the size of the recirculation zone and move the shear layer reattachment point further upstream. The combination of these effects results in the largest momentum flux through the control volume, and thus the greatest drag for the nozzle case. It is noted that the opposite trends occur for the diffuser, where the flow streamlines tend to diverge away from the aft ramp. This will ultimately mitigate flow stagnation on the ramp, and thus mitigates drag penalties. Similar to discussions in the literature [29], the drag on the cavity is a function of the shear layer reattachment point. However, both the cavity drag and shear layer reattachment are a function of the mean pressure gradient. Regarding the accuracy of the momentum flux and drag analysis, it is possible that a higher vector resolution (approaching the Kolmogorov scales) would broaden the distribution of local momentum flux and shear stress values around the mean values presented. However, we are confident that ensemble averaging across the control surface (which contains >200 vectors) and all temporal realizations (>5000 samples) accurately capture the trend of increasing drag as the mean pressure gradient shifts from adverse to favorable. The trends are also supported by the flow streamlines and entrainment dynamics based on the mean flow contours.

3.2. Self-sustained oscillations

The stability characteristics and mean drag presented in the previous section are dependent on the flow dynamics through the cavity. In general, flow over a cavity will experience periodic self-sustained oscillations, which imparts pressure, velocity, and density fluctuations, and ultimately results in drag penalties [29]. Additionally, oscillations induced by aerodynamic instabilities, such as Kelvin-Helmholtz or von-Kármán vortex shedding, will play an integral role in flame stabilization and blowoff dynamics [51,62–64]. For this reason, this section quantifies the oscillations experienced by the flame and flow field to better understand the influence of the pressure gradient on reacting cavity dynamics.

Instantaneous flame and flow contours for each test configuration are provided in Fig. 8. The instantaneous flame front contours were extracted from the instantaneous PIV images to provide a more practical two-dimensional representation of the local flame structure in the same plane as the velocity measurements [65]. The instantaneous flame fronts shown in Fig. 8 are comprised of small-scale structures due to turbulent shear layer dynamics that sustain ignition. At any given axial position, the flame will undergo temporal oscillations. The instantaneous transverse (y) flame position at $x/H = 1$, 2, and 3 is documented through time, and a spectral analysis is performed on this signal using a Welch method [66], which relies on a Fourier transform to quantify oscillation frequencies. The resulting spectra for each test configuration is provided in Fig. 9. In general, the flame spectra for all test cases are similar to a turbulence cascade. However, the transition from an adverse pressure gradient to an increasing favorable pressure gradient is accompanied with the emergence of a spectral peak, which means that the flame is locking into a distinct oscillation mode. More specifically, the diffuser configuration depicts a very weak spectral peak near $f \approx 630$ Hz, the nominal configuration has a more notable peak at $f \approx 550$ Hz, and the nozzle has a high amplitude peak at $f \approx 520$ Hz. The higher energy peaks above 1000 Hz are harmonic modes of the flame oscillation that have been
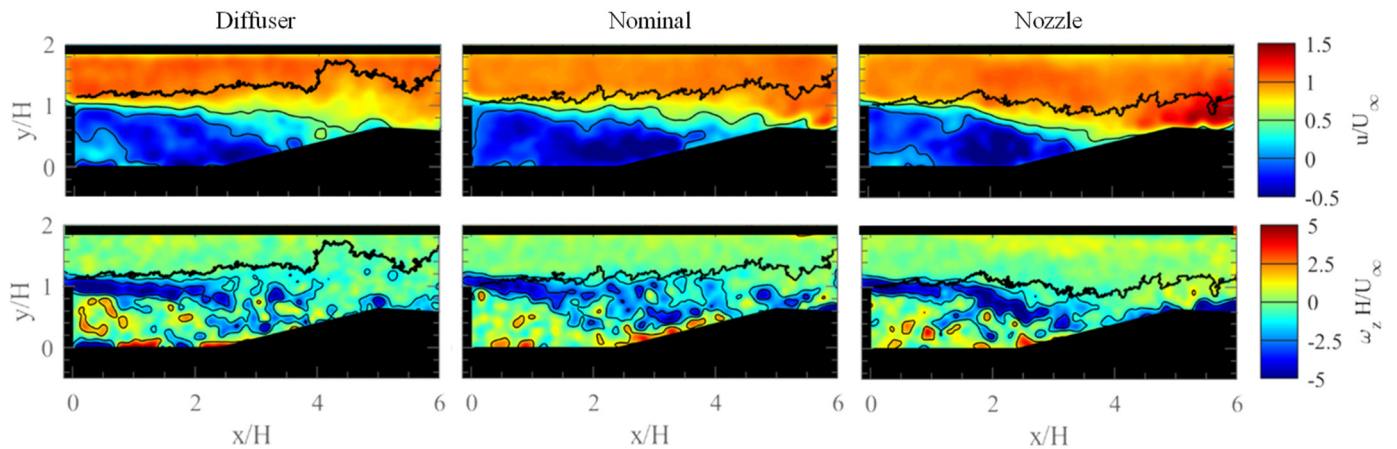
Fig. 8. Instantaneous contours of streamwise velocity (top row) and spanwise vorticity (bottom row) for the different test configurations. All contours are overlayed with the instantaneous flame front.
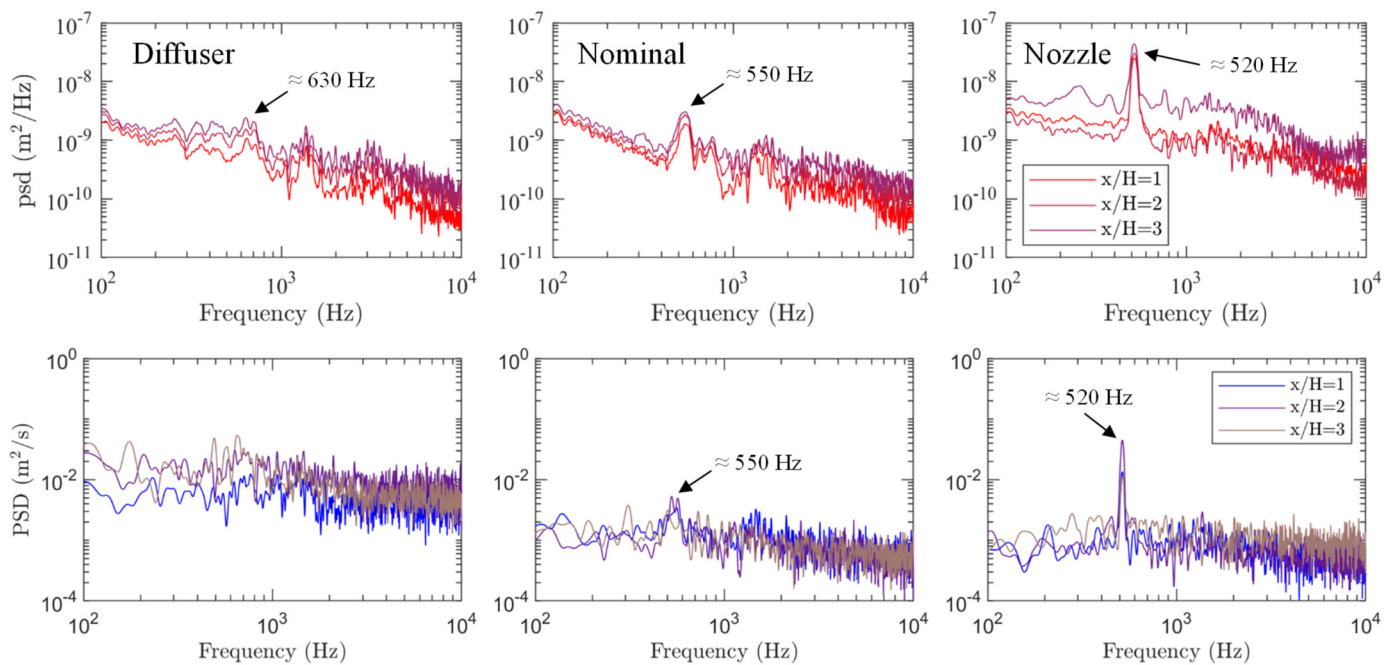
Fig. 9. Spectra of transverse flame oscillations (top row) and the transverse velocity in the shear layer (bottom row) at axial locations $x/H = 1$, 2, and 3.

shown to produce amplitude peaks at frequencies $2f$, $3f$, and so on [51,62,67,68].

The differences in flame oscillations for each mean pressure gradient are expected to be driven by the cavity flow field dynamics. To quantify the flow oscillations, a spectral analysis is conducted on the transverse velocity taken in the shear layer region at locations $x/H = 1$, 2, and 3. An example of the positions probed for the spectral analysis in the shear layer are also provided in the mean vorticity contour in Fig. 4c, and the resulting spectra for each case is included in Fig. 9. It is first noted that the shear layer depicts broadband energy distributed between 1000–5000 Hz. This is expected, since the separating shear layer acts as a source of turbulence which has not yet evolved into a fully developed turbulent flow with a Kolmogorov-type energy cascade [69]. Thus, the turbulence is not well developed in the shear layer, and the profiles in Fig. 9 do not show a notable cascade. However, the peak frequencies in the shear layer spectra match the peaks observed in the flame spectra. This confirms that the flame oscillations are indeed driven from the aerodynamic instabilities in the cavity. Additionally, the trend toward a lower frequency, higher amplitude

oscillation is linked with a shift from an adverse to a favorable pressure gradient. In this case, the transition to a favorable pressure gradient was shown to increase the freestream velocities in the cavity and simultaneously decrease the length of the recirculation zone and shear layer reattachment point. However, the increased velocity will also collimate the flame, and push the flame front closer to the shear layer. Thus, the flame becomes more exposed to the shear layer and the transverse oscillations become more pronounced for the nozzle case. However, it remains important to discern the underlying mechanisms that drive the specific oscillation frequencies observed in Fig. 9.

A non-reacting flow over a closed cavity will experience large-scale vortex shedding which is characterized by a Strouhal number of $St = fH/u_\infty = 0.1$ [70]. For the reacting flows investigated here, the nominal shear layer oscillations have a small peak at 530 Hz, which corresponds to $St = 0.1$. This provides a strong indication that the oscillation frequencies witnessed in Fig. 9 are a suppressed mode of vortex shedding that would occur under nonreacting conditions.
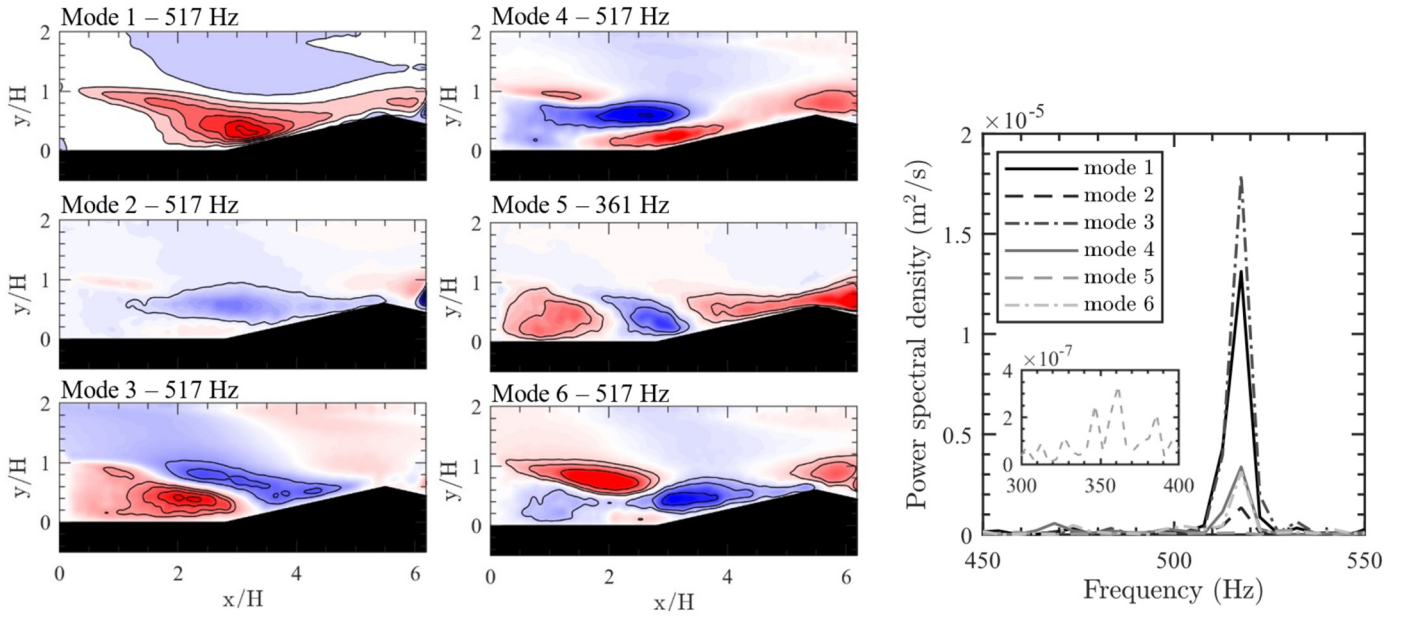
Fig. 10. The first 6 modes obtained from proper orthogonal decomposition (POD) of the streamwise velocity for the nozzle case along with the corresponding spectra from POD.

3.3. Proper orthogonal decomposition

To visualize the flow structures associated with the $St = 0.1$ flow oscillations, proper orthogonal decomposition (POD) is performed on the streamwise velocity fields. POD is a technique that identifies coherent structures in time-resolved data series. The advantage of POD is that it is a data driven technique, which can be used to characterize turbulent flow instabilities, and the extracted structures can be used to build reduced order models of turbulent flows. The primary limitation of POD analysis is the order reduction from higher-dimensional space to lower-dimensional space. This becomes particularly relevant for the reduced order modeling of turbulent flows, where vector valued eigenfunctions effectively constrain the relative magnitudes of the components of fluid velocity fields, which can result in the prediction of non-physical behaviors [71]. Despite the linear nature of POD, feature extraction can still be accomplished from nonlinear Navier Stokes based problems, and have been shown to capture coherent structures with a reasonable degree of accuracy [72]. The application of POD has also been extended to turbulent reacting flows, and has been used across a variety of flameholder configurations [73–75].

The mathematical formulation to extract POD modes is outlined in Eq. (9). Instantaneous velocity fields are first compiled into column vectors $\vec{x}^{(i)}$. The column vectors are arranged into an $N \times M$ matrix, X, where N is the number of instantaneous snapshots and M is the total number of data points contained in a single snapshot. The average value of the reshaped data matrix is subtracted from itself to form the matrix Y, and a singular value decomposition is performed on Y. The output of the singular value decomposition provides three matrices: U, Σ, and V^*. The U matrix contains the eigenvectors of Y and contains the POD modes. V represents the temporal evolution of each mode, and Σ is a diagonal matrix based on the rank of the POD modes. Each of the matrices is arranged hierarchically based on each modes energy content in the data.

$$\vec{x}^{(i)} = \begin{bmatrix} x_1^{(i)} \\ x_2^{(i)} \\ x_3^{(i)} \\ \vdots \\ x_M^{(i)} \end{bmatrix} \tag{9a}$$

$$X = \begin{bmatrix} \vec{x}^{(1)} \vec{x}^{(2)} \vec{x}^{(3)} \cdots \vec{x}^{(N)} \end{bmatrix} \tag{9b}$$

$$Y = X - \overline{X} \tag{9c}$$

$$Y \approx U\Sigma V^* \tag{9d}$$

To visualize the coherent structures associated with the dominant flow oscillations, POD is performed on the streamwise velocity field for the nozzle case, since the nozzle presented the most well-defined oscillatory peak. The first 6 POD modes are provided in Fig. 10, along with the corresponding spectra for the 6 modes. It is noted that the POD for the other two cases produced similar structures shown here but at frequencies near their respective peaks in Fig. 9. However, the POD spectra have less defined peaks, and the energy is distributed across a wider range of frequencies compared to the nozzle case. For the nozzle case presented in Fig. 10, all modes, except for mode 5, capture the same dominant peak as the previous spectral analysis. Modes 1 and 2 capture time-averaged flow features. In particular, mode 1 captures the time-averaged shear layer region. Mode 3 depicts a large-scale separation between the shear layer region and the recirculating flow region. Modes 4 and 6 catch large-scale structures in the cavity region, and mode 6 tends to highlight regions of high and low streamwise velocity. Among all presented modes, the most pertinent trend is that the entire cavity region is encompassed by the large-scale oscillation. Modes 3–6 all depict structures with axial length scales on the order of L or $L/2$, and transverse length scales on the order of the cavity height H or $H/2$. The orientation and length scales of the energetic structures, combined with the Strouhal number, reinforces that the oscillations are likely the manifestation of a vortex shedding mode typically observed under non-reacting flow conditions.

3.4. Pressure gradient effects on oscillation frequency

The manner in which the pressure gradient and the exothermic reaction influence the flame and flow oscillation frequencies can be described by the vorticity transport equation [76–78]:

$$\frac{\partial \omega_i}{\partial t} + u_k \frac{\partial \omega_i}{\partial x_k} = \underbrace{S_{ij}\omega_j}_{\text{I}} - \underbrace{S_{jj}\omega_i}_{\text{II}} + \underbrace{\epsilon_{ijk}\frac{1}{\rho^2}\frac{\partial \rho}{\partial x_j}\frac{\partial P}{\partial x_k}}_{\text{III}} - \underbrace{\epsilon_{ijk}\frac{1}{\rho^2}\frac{\partial \rho}{\partial x_k}\frac{\partial \tau_{kl}}{\partial x_l}}_{\text{IV}}$$
$$+ \underbrace{\nu \frac{\partial^2 \omega_i}{\partial x_k}}_{\text{V}}. \qquad (10)$$

Under non-reacting flow conditions, large scale vortices will periodically shed off of the trailing edge of the cavity [70]. The advection and evolution of these vortices are controlled by two key mechanisms: the vortex stretching term (term I) and viscous transport terms (term V). However, previous studies have shown that increasing the favorable pressure gradient by decreasing the cross-sectional flow area leads to smaller vortex shedding frequencies under nonreacting conditions [79]. With respect to the vorticity mechanisms above, the decrease in cross-sectional area should minimize large-scale vortex stretching effects, while significant axial flow acceleration will induce a streamwise gradient $\partial u / \partial x$. This will propagate onto the S_{jj} term, and thus activate the dilatation mechanism (term II). Based on the convention in Eq. (10), an increase in S_{jj} from axial flow acceleration will dampen vorticity, and likely causes vortex shedding frequency to decrease with flow confinement.

A similar trend is observed for the reacting conditions explored here. However, the flames heat release will drive gas expansion effects, which further suppress the vortex shedding instability by augmenting the dilatation mechanism. Under reacting conditions, the heat released from the flame will also activate the baroclinic torque (term III), which generates significant vorticity from misaligned density gradients across the flame and pressure gradients in the flow field. The baroclinic torque will produce vorticity along the length of the flame in an opposing direction as the shear layer generated vorticity [63,80]. As such, the baroclinicity acts to dampen the shear layer vorticity magnitudes [51], but will also induce a slight shift in shear layer oscillation frequencies [79]. Therefore, the combined effects of flow dilatation and baroclinic torque are considered the primary source for the different peak frequencies observed among the three pressure gradient configurations.

4. Discussion

The above results regarding the influence of the mean pressure gradient on flame-flow performance in a cavity combustor are analogous to relationships found in literature. For instance, both experimental [30,81] and numerical [30,82] cavity studies have shown that the drag coefficient and stagnation pressure losses are mitigated by decreasing the angle of the aft ramp from a 90° baseline condition. A similar phenomenon is observed here; however, rather than altering the angle of the aft ramp, this study alters the orientation of the wall opposite of the cavity. Both methodologies produce a similar effect, where the relative angle between the freestream flow and the aft ramp are coupled with the mean drag on the cavity. In both studies, the mean cavity drag decreases as the freestream flow becomes more aligned (or more parallel) with the angle of the aft ramp.

Increased drag on the cavity was also coupled with the emergence of a well-defined and energetic oscillation mode. This is also similar to discussions in literature [29], which suggest that strong cavity oscillations are coupled with increased drag penalties. In this case, it is possible to mitigate cavity oscillations and drag by allowing the flow to diffuse and inducing an adverse pressure gradient in the cavity. However, this is accompanied with decreased streamwise momentum. Thus, there is a tradeoff between kinetic energy conversion efficiencies for thrust production, and the mean drag on the cavity.

Additionally, the increase in the mean favorable pressure gradient will increase freestream flow velocities, and subsequently decrease the mean inclination angle of the flame. This will ultimately subject the flame to larger aerodynamic strain rates while simultaneously causing the flame to interact with the inflection point. Combined, these effects make it more prone for the flame to extinguish [5]. Therefore, increased momentum production from flow confinement not only increases the mean drag on the cavity, but also reduces the safe operability window in which the flame can be stabilized. The reduced stability window was also realized from the decrease in the mean recirculation zone length and residence time quantities presented above. In this manner, altering the mean pressure gradient by manipulating the angle of the wall opposite of the cavity provides an alternative solution to tailor the performance of high-speed ramjet combustors without intricate mechanical alterations to the cavity geometry.

5. Conclusions

The performance of ramjet cavity stabilized flames under the influence of mean pressure gradients was explored through chemiluminescence flame imaging and particle image velocimetry. The mean pressure gradient was altered by changing the angle of the wall opposite of the cavity. Imposing a mean favorable pressure gradient was shown to reduce the length of the recirculation zone and decrease the corresponding residence time. This pushed the shear layer reattachment point further upstream, and was coupled with an increased momentum flux into the cavity. The increased velocity and momentum flux in the cavity resulted in larger drag penalties as the mean pressure gradient shifted from adverse to favorable.

The oscillatory dynamics of the flame and flow field were investigated through Fourier transform and proper orthogonal decomposition methods. For the case with the adverse pressure gradient, the flame spectra depicted a very weak oscillation peak. The transition to a stronger favorable pressure gradient decreased the dominant oscillation frequency, but increased the amplitude of oscillations as the spectra coalesced into a narrowband peak. The oscillations collapsed to a Strouhal number of $St = 0.1$, which is a suppressed mode of vortex shedding that would be present under non-reacting flow conditions. This was further confirmed by POD analysis for the nozzle configuration, where large-scale coherent structures were found to occupy the entire cavity region, which is expected for vortex shedding instabilities.

The above results demonstrate that the propulsive performance, cavity drag, and turbulent oscillation dynamics can be controlled via the mean axial pressure gradient. In this case, a tradeoff between axial momentum and flame stability/cavity drag was found. Thus, the mean pressure gradient can be used to tailor the performance of ramjet-style combustors, which is a mechanically simple alternative design strategy which does not rely on geometric manipulations of the cavity itself.

Declaration of competing interest

The authors declare that they have no known competing financial interests or personal relationships that could have appeared to influence the work reported in this paper.

Data availability

No data was used for the research described in the article.

Acknowledgements

References

[1] M.J. Turner, R.W. Clough, L.J. Topp, Hypersonic flight and the Re-entry problem, Aeronaut. Sci. 25 (1958).

[2] D.A. Rosato, M. Thornton, J. Sosa, C. Bachman, G.B. Goodwin, K.A. Ahmed, Stabilized detonation for hypersonic propulsion, Proc. Natl. Acad. Sci. USA 118 (2021) 1–7, https://doi.org/10.1073/pnas.2102244118.

[3] T. Kanda, Combined-cycle engines, Encycl. Aerosp. Eng. (2010) 1–10, https://doi.org/10.1002/9780470686652.eae114.

[4] W. Huang, Z. Du bo, L. Yan, R. Moradi, Flame propagation and stabilization in dual-mode scramjet combustors: a survey, Prog. Aerosp. Sci. 101 (2018) 13–30, https://doi.org/10.1016/j.paerosci.2018.06.003.

[5] F.W. Barnes, C. Segal, Cavity-based flameholding for chemically-reacting supersonic flows, Prog. Aerosp. Sci. 76 (2015) 24–41, https://doi.org/10.1016/j.paerosci.2015.04.002.

[6] Q. Liu, D. Baccarella, W. Landsberg, A. Veeraragavan, T. Lee, Cavity flameholding in an optical axisymmetric scramjet in Mach 4.5 flows, Proc. Combust. Inst. 37 (2019) 3733–3740, https://doi.org/10.1016/j.proci.2018.08.037.

[7] A.J. Morales, J. Reyes, I. Boxx, K.A. Ahmed, The effects of turbulence on the lean blowout mechanisms of bluff-body flames, Proc. Combust. Inst. 38 (2020) 6317–6325, https://doi.org/10.1016/j.proci.2020.06.138.

[8] B.R. Chowdhury, B.M. Cetegen, Effects of fuel properties and free stream turbulence on characteristics of bluff-body stabilized flames, Combust. Flame 194 (2018) 206–222, https://doi.org/10.1016/j.combustflame.2018.04.027.

[9] D. Ballal, A.H. Lefebvre, Weak extinction limits of turbulent flowing mixtures, J. Eng. Power 101 (1979) 343–348.

[10] E.E. Zukoski, F.E. Marble, Experiments concerning the mechanism of flame blowoff from bluff bodies, Proc. Gas Dyn. Symp. (1956) 205–210.

[11] L. Ma, Q. Lei, Y. Wu, W. Xu, T.M. Ombrello, C.D. Carter, From ignition to stable combustion in a cavity flameholder studied via 3D tomographic chemiluminescence at 20 kHz, Combust. Flame 165 (2016) 1–10, https://doi.org/10.1016/j.combustflame.2015.08.026.

[12] D.A. Rosato, T.M. Ombrello, D. Cuppoletti, C.D. Carter, S.D. Hammack, K.A. Ahmed, Ignition mechanisms of pulse detonator initiated scramjet cavity, Proc. Combust. Inst. 38 (2021) 3853–3860, https://doi.org/10.1016/j.proci.2020.07.065.

[13] P. Xiong, D. Zheng, Y. Tan, Y. Tian, J. Le, Experimental study of ignition and combustion characteristics of ethylene in cavity-based supersonic combustor at low stagnation temperature and pressure, Aerosp. Sci. Technol. 109 (2021) 106414, https://doi.org/10.1016/j.ast.2020.106414.

[14] E. Hassan, T.M. Ombrello, D.M. Peterson, Computational and experimental investigation of ignition in a Mach 2 cavity-based flameholder, Aerosp. Sci. Technol. 115 (2021) 106756, https://doi.org/10.1016/j.ast.2021.106756.

[15] N. Yokev, H.E. Brod, D. Cao, D. Michaels, Impact of fuel injection distribution on flame holding in a cavity-stabilized scramjet, J. Propuls. Power 37 (2021) 584–594, https://doi.org/10.2514/1.B38093.

[16] H. Sitaraman, S. Yellapantula, M.T. Henry de Frahan, B. Perry, J. Rood, R. Grout, M. Day, Adaptive mesh based combustion simulations of direct fuel injection effects in a supersonic cavity flame-Holder, Combust. Flame 232 (2021) 111531, https://doi.org/10.1016/j.combustflame.2021.111531.

[17] G. Choubey, K.M. Pandey, Effect of variation of inlet boundary conditions on the combustion flow-field of a typical double cavity scramjet combustor, Int. J. Hydrog. Energy 43 (2018) 8139–8151, https://doi.org/10.1016/j.ijhydene.2018.03.062.

[18] W.O. Landsberg, D. Curran, A. Veeraragavan, Experimental flameholding performance of a scramjet cavity with an inclined front wall, Aerosp. Sci. Technol. 126 (2022) 107622, https://doi.org/10.1016/j.ast.2022.107622.

[19] Y. Zhao, X. He, J. Xiao, M. Li, Effect of cavity-air injection mode on the performance of a trapped vortex combustor, Aerosp. Sci. Technol. 106 (2020) 106183, https://doi.org/10.1016/j.ast.2020.106183.

[20] J. Miao, Y. Fan, W. Wu, S. Zhao, Influence of air-entraining intensity on the afterburner ignition, flame-holding and combustion characteristics, Aerosp. Sci. Technol. 106 (2020) 106063, https://doi.org/10.1016/j.ast.2020.106063.

[21] H. Wang, X. Song, L. Li, Y. Huang, M. Sun, Lean blowoff behavior of cavity-stabilized flames in a supersonic combustor, Aerosp. Sci. Technol. 109 (2021) 106427, https://doi.org/10.1016/j.ast.2020.106427.

[22] K. Yang, N. Wang, Y. Pan, Z.G. Wang, C. yang Liu, X.P. Li, Effect of cavity arrangement on the ignition mode of vaporized kerosene in supersonic flow, Aerosp. Sci. Technol. 113 (2021) 106691, https://doi.org/10.1016/j.ast.2021.106691.

[23] R.S. Gabruk, L.A. Roe, Velocity characteristics of reacting and nonreacting flows in a dump combustor, J. Propuls. Power 10 (1994) 148–154, https://doi.org/10.2514/3.23723.

[24] R.W. Pitz, J.W. Daily, Combustion in a turbulent mixing layer formed at a rearward-facing step, AIAA J. 21 (1983) 1565–1570, https://doi.org/10.2514/3.8290.

[25] H.M. Nicholson, J.P. Field, Some experimental techniques for the investigation of the mechanism of flame stabilization in the wakes of bluff bodies, Proc. Combust. Inst. 3 (1948) 44–68.

[26] J.P. Longwell, J.E. Chenevey, W.W. Clark, E. Frost, Flame stabilization by baffles in a high velocity gas stream, Proc. Combust. Inst. 3 (1948) 40–44.

[27] J.P. Longwell, E.E. Frost, M.A. Weiss, Flame stability in bluff body recirculation zones, Ind. Eng. Chem. 1. 45 (1953) 1629–1633.

[28] L.W. Huellmantel, R.W. Ziemer, A.B. Cambel, Stabilization of premixed propane-air flames in recessed ducts, Jet Propuls. 27 (1957) 31–34, https://doi.org/10.2514/8.12565.

[29] A. Ben-Yakar, R.K. Hanson, Cavity flame-holders for ignition and flame stabilization in scramjets: an overview, J. Propuls. Power 17 (2001) 869–877.

[30] M.R. Gruber, R.A. Baurle, T. Mathur, K.Y. Hsu, Fundamental studies of cavity-based flameholder concepts for supersonic combustors, J. Propuls. Power 17 (2001) 146–153, https://doi.org/10.2514/2.5720.

[31] X. Liu, M. Barzegar Gerdroodbary, M. Sheikholeslami, R. Moradi, A. Shafee, Z. Li, Effect of strut angle on performance of hydrogen multi-jets inside the cavity at combustion chamber, Int. J. Hydrog. Energy 45 (2020) 31179–31187, https://doi.org/10.1016/j.ijhydene.2020.08.124.

[32] S. Lakka, P. Randive, K.M. Pandey, Implication of geometrical configuration of cavity on combustion performance in a strut-based scramjet combustor, Acta Astronaut. 178 (2021) 793–804, https://doi.org/10.1016/j.actaastro.2020.08.040.

[33] M. Li, X. He, Y. Zhao, Y. Jin, Z. Ge, W. Huang, Effect of strut length on combustion performance of a trapped vortex combustor, Aerosp. Sci. Technol. 76 (2018) 204–216, https://doi.org/10.1016/j.ast.2018.02.019.

[34] C.C. Rasmussen, J.F. Driscoll, K.Y. Hsu, J.M. Donbar, M.R. Gruber, C.D. Carter, Stability limits of cavity-stabilized flames in supersonic flow, Proc. Combust. Inst. 30 (2005) 2825–2833, https://doi.org/10.1016/j.proci.2004.08.185.

[35] C. Liu, Z. Wang, M. Sun, H. Wang, P. Li, Characteristics of a cavity-stabilized hydrogen jet flame in a model scramjet combustor, AIAA J. 57 (2019) 1624–1635, https://doi.org/10.2514/1.J057346.

[36] J.L. Ruan, P. Domingo, G. Ribert, Analysis of combustion modes in a cavity based scramjet, Combust. Flame 215 (2020) 238–251, https://doi.org/10.1016/j.combustflame.2020.01.034.

[37] Z. Wang, H. Wang, M. Sun, Review of cavity-stabilized combustion for scramjet applications, Proc. Inst. Mech. Eng., G J. Aerosp. Eng. 228 (2014) 2718–2735, https://doi.org/10.1177/0954410014521172.

[38] M.R. Gruber, J.M. Donbar, C.D. Carter, K.Y. Hsu, Mixing and combustion studies using cavity-based flameholders in a supersonic flow, J. Propuls. Power 20 (2004) 769–778, https://doi.org/10.2514/1.5360.

[39] O.W. McGregor, R.A. White, Drag of rectangular cavities in supersonic and transonic flow including the effects of cavity resonance, AIAA J. 8 (1970) 1959–1964, https://doi.org/10.2514/3.6032.

[40] C.J. Rising, G.B. Goodwin, R.F. Johnson, D.A. Kessler, J. Sosa, M. Thornton, K.A. Ahmed, Numerical investigation of turbulent flame-vortex interaction in premixed cavity stabilized flames, Aerosp. Sci. Technol. 129 (2022) 107805, https://doi.org/10.1016/j.ast.2022.107805.

[41] M. Raffel, C.E. Willert, S.T. Wereley, J. Kompenhans, Particle Image Velocimetry A Practical Guide, second ed., Springer, New York, 2018.

[42] A.H. Rauch, H.K. Chelliah, On the ambiguity of premixed flame thickness definition of highly pre-heated mixtures and its implication on turbulent combustion regimes, Combust. Theory Model. 24 (2020) 573–588, https://doi.org/10.1080/13647830.2020.1722857.

[43] P.A. Davidson, Turbulence: An Introduction for Scientists and Engineers, Oxford University Press, 2004.

[44] A.N. Kolmogorov, The local structure of turbulence in incompressible viscous fluid for very large Reynolds numbers, Dolk. Akad. Nauk SSSR 30 (1941) 299–303.

[45] A. Melling, Tracer particles and seeding for particle image velocimetry, Meas. Sci. Technol. 8 (1997) 1406–1416.

[46] B. Wieneke, PIV uncertainty quantification from correlation statistics, Meas. Sci. Technol. 26 (2015), https://doi.org/10.1088/0957-0233/26/7/074002.

[47] S. Pfadler, F. Dinkelacker, F. Beyrau, A. Liepertz, High resolution dual-plane stereo-PIV for validation of subgrid scale models in large-eddy simulations of turbulent premixed flames, Combust. Flame 156 (2009) 1552–1564.

[48] Y. Zheng, L. Weller, S. Hochgreb, 3D flame surface density measurements via orthogonal cross-planar mie scattering in a low-turbulence bunsen flame, Proc. Combust. Inst. 39 (2022) 2369–2377, https://doi.org/10.1016/j.proci.2022.07.076.

[49] L. Ma, Y. Wu, Q. Lei, W. Xu, C.D. Carter, 3D flame topography and curvature measurements at 5 kHz on a premixed turbulent busen flame, Combust. Flame 166 (2016) 66–75.

[50] A.J. Morales, M. Thornton, T. Genova Jr., M. Tonarely, K.A. Ahmed, The role of flow confinement on turbulent kinetic energy transfer across premixed flames, Combust. Flame 241 (2022) 112103, https://doi.org/10.1016/j.combustflame.2022.112103.

[51] A.J. Morales, I.M. Lasky, M.K. Geikie, C.A. Engelmann, K.A. Ahmed, Mechanisms of flame extinction and lean blowout of bluff body stabilized flames, Combust. Flame 203 (2019), https://doi.org/10.1016/j.combustflame.2019.02.002.

[52] N. Otsu, A threshold selection method from gray-level histograms, IEEE Trans. Syst. Man Cybern. 9 (1979) 62–66.

[53] G.A. Moore, Automatic scanning and computer processes for the quantative analysis of micrographs and equivalent subjects, in: Pictoral Pattern Recognit., 1968, pp. 275–362.

[54] F.N. Egolfopoulos, D.L. Zhu, C.K. Law, Experimental and numerical determination of laminar flame speeds: mixtures of C2-hydrocarbons with oxygen and nitrogen, Symp. Combust. 23 (1991) 471–478, https://doi.org/10.1016/S0082-0784(06)80293-6.

[55] M.I. Hassan, K.T. Aung, O.C. Kwon, G.M. Faeth, Properties of laminar premixed hydrocarbon/air flames at various pressures, J. Propuls. Power 14 (1998) 479–488, https://doi.org/10.2514/2.5304.

[56] G. Jomaas, X.L. Zheng, D.L. Zhu, C.K. Law, Experimental determination of counterflow ignition temperatures and laminar flame speeds of C2-C3 hydrocarbons at atmospheric and elevated pressures, Proc. Combust. Inst. 30 (2005) 193–200, https://doi.org/10.1016/j.proci.2004.08.228.

[57] H. Wang, Z. Wang, M. Sun, N. Qin, Experimental and numerical investigation of cavity-based supersonic flow and combustion, Proc. Inst. Mech. Eng., G J. Aerosp. Eng. 228 (2014) 781–798, https://doi.org/10.1177/0954410013480300.

[58] M. Gharib, A. Roshko, The effect of flow oscillations on cavity drag, J. Fluid Mech. 177 (1987) 501–530, https://doi.org/10.1017/S002211208700106X.

[59] R.W. Fox, P.J. Prichard, A.T. McDonald, Introduction to Fluid Mechanics, seventh ed., John Wiley & Sons, New York, NY, 2010.

[60] S.R. Turns, An Introduction to Combustion: Concepts and Applications, McGraw-Hill, 2000.

[61] S. Gordon, B.J. McBride, Computer program for calculation of complex chemical equilibrium compositions and applications, NASA Ref. Publ. 1311 (1996).

[62] S.J. Shanbhogue, S. Husain, T. Lieuwen, Lean blowoff of bluff body stabilized flames: scaling and dynamics, Prog. Energy Combust. Sci. 35 (2009) 98–120.

[63] B. Emerson, J. O'connor, M. Juniper, T. Lieuwen, Density ratio effects on reacting bluff-body flow field characteristics, J. Fluid Mech. 706 (2012) 219–250.

[64] S.G. Tuttle, S. Chaudhuri, K.M. Kopp-Vaughan, T.R. Jensen, Lean blowoff behavior of assymetrically-fueled bluff body-stabilized flames, Combust. Flame 160 (2013) 1677–1692.

[65] S. Pfadler, F. Beyrau, A. Leipertz, Flame front detection and characterization using conditioned particle image velocimetry, Opt. Express 15 (2007) 15444–15456.

[66] P. Welch, The use of fast Fourier transform for the estimation of power spectra: a method based on time averaging over short, modified periodograms, IEEE Trans. Audio Electroacoust. 15 (1967) 70–73.

[67] A. Prasad, C.H.K. Williamson, The instability of the shear layer seperating from a bluff body, J. Fluid Mech. 333 (1997) 375–402.

[68] Y. Yalcinkaya, A.G. Gungor, Pressure gradient effect on flame-vortex interaction in lean premixed bluff body stabilized flames, Phys. Fluids 35 (2023) 045105.

[69] V. Statnikov, T. Sayadi, M. Meinke, P. Schmid, W. Schröder, Analysis of pressure perturbation sources on a generic space launcher after-body in supersonic flow using zonal turbulence modeling and dynamic mode decomposition, Phys. Fluids 27 (2015), https://doi.org/10.1063/1.4906219.

[70] D. Wee, T. Yi, A. Annaswamy, A.F. Ghoniem, Self-sustained oscillations and vortex shedding in backward-facing step flows: simulation and linear instability analysis, Phys. Fluids 16 (2004) 3361–3373, https://doi.org/10.1063/1.1773091.

[71] T.R. Smith, J. Moehlis, P. Holmes, Low-dimensional modelling of turbulence using the proper orthogonal decomposition: a tutorial, Nonlinear Dyn. 41 (2005) 275–307.

[72] G. Berkooz, P. Holmes, J.L. Lumley, The proper orthogonal, decomposition in the analysis of turbulent flows, Annu. Rev. Fluid Mech. 25 (1993) 539–575, https://doi.org/10.1146/annurev.fluid.25.1.539.

[73] S. Kostka, A.C. Lynch, B.C. Huelskamp, B.V. Kiel, J.R. Gord, S. Roy, Characterization of flame-shedding behavior behind a bluff-body using proper orthogonal decomposition, Combust. Flame 159 (2012) 2872–2882, https://doi.org/10.1016/j.combustflame.2012.03.021.

[74] A.J. Morales, T. Genova, J. Reyes, I. Boxx, K.A. Ahmed, Turbulence-driven blowout instabilities of premixed bluff-body flames, Flow Turbul. Combust. 108 (2022) 213–236, https://doi.org/10.1007/s10494-021-00269-8.

[75] D.M. Markovich, S.S. Abdurakipov, L.M. Chikishev, V.M. Dulin, K. Hanjalić, Comparative analysis of low- and high-swirl confined flames and jets by proper orthogonal and dynamic mode decompositions, Phys. Fluids 26 (2014), https://doi.org/10.1063/1.4884915.

[76] C. Dopazo, L. Cifuentes, N. Chakraborty, Vorticity budgets in premixed combusting turbulent flows at different Lewis numbers, Phys. Fluids 29 (2017) 1–14, https://doi.org/10.1063/1.4981219.

[77] A.N. Lipatnikov, S. Nishiki, T. Hasegawa, A direct numerical simulation study of vorticity transformation in weakly turbulent premixed flames, Phys. Fluids 26 (2014) 1–16, https://doi.org/10.1063/1.4898640.

[78] N. Chakraborty, I. Konstantinou, A. Lipatnikov, Effects of Lewis number on vorticity and enstrophy transport in turbulent premixed flames, Phys. Fluids 28 (2016), https://doi.org/10.1063/1.4939795.

[79] A.J. Morales, J. Reyes, P.H. Joo, I. Boxx, K.A. Ahmed, Pressure gradient tailoring effects on the mechanisms of bluff-body flame extinction, Combust. Flame 215 (2020) 224–237, https://doi.org/10.1016/j.combustflame.2020.01.035.

[80] M.K. Geikie, Z.R. Carr, K.A. Ahmed, D.J. Forliti, On the flame-generated vorticity dynamics of bluff-body-stabilized premixed flames, Flow Turbul. Combust. 99 (2017) 487–509.

[81] S. Jeyakumar, S.M. Assis, K. Jayaraman, Effect of axisymmetric aft wall angle cavity in supersonic flow field, Int. J. Turbo Jet-Engines 35 (2018) 29–34, https://doi.org/10.1515/tjj-2016-0027.

[82] X. Zhang, A. Rona, J.A. Edwards, The effect of trailing edge geometry on cavity flow oscillation driven by a supersonic shear layer, Aeronaut. J. 102 (1998) 129–135.